

Composition and crystallography dependence of the work function: Experiment and calculations of Pt-Al alloys

Lior Kornblum,* Pini Shekhter, Yair Slovatzky, Yaron Amouyal, and Moshe Eizenberg

Department of Materials Science & Engineering, Technion—Israel Institute of Technology, Haifa 32000, Israel

(Received 3 July 2012; revised manuscript received 13 August 2012; published 5 September 2012)

The work function (WF) of several phases of Pt-Al alloys is investigated. A first-principles study is performed to determine the dependence of the vacuum WF (VWF) on the phase, crystallographic orientation, and atomic termination. In parallel, the effective WF (EWF) of these alloys is experimentally measured using metal-oxide semiconductor devices. A detailed microstructural characterization based on x-ray diffraction and transmission electron microscopy allows the comparison between experiment and calculations. It is found that despite the formation of a complex microstructure, the calculated VWF values are in good agreement with the experimental EWF values. The possible VWF range for each phase has a relatively small (~ 0.5 eV) span for different orientations and atomic terminations, and it is found that Pt atoms in the terminating plane are more dominant than Al atoms. The results demonstrate that first-principles calculations of the WF of alloys can be used to successfully predict the experimental WF and that knowledge of the microstructure is important for the accuracy of these calculations.

DOI: [10.1103/PhysRevB.86.125305](https://doi.org/10.1103/PhysRevB.86.125305)

PACS number(s): 73.30.+y, 73.61.At, 65.40.gh, 68.35.bd

I. INTRODUCTION

The work function (WF) of metals plays an important role in several different fields, including corrosion and catalysis,^{1,2} chemical sensing,³ electron sources,⁴ and Schottky contacts.⁵ In the recent decade, a significant interest in the WF of metals was triggered by the investigation of metal gate electrodes for the metal-oxide semiconductor (MOS) technology, which is the basis for most modern electronics.

The downscaling of the physical dimensions of MOS devices is the key to the advancement of this technology. In recent years, the scaling requirements have dictated the replacement of the traditional polycrystalline Si gate and SiO₂ dielectric with metal gates over high dielectric constant, the so called “high-k” dielectrics.^{6,7} The work function of the gate electrode is the key parameter for controlling the threshold voltage of devices, which is a crucial parameter for their performance.

In the early days of high-k/metal gate (HK/MG), many devices showed unexpected discrepancies between the WF of the gate and the behavior of the device. This has led to the definition of the effective work function (EWF), which means the gate’s WF as effectively sensed from the semiconductor’s side of an MOS device.⁸ To distinguish the classical WF from the EWF, the former parameter is commonly termed the vacuum work function (VWF). These WF discrepancies are often discussed in terms of a Fermi level pinning (FLP) phenomenon,⁹ and several physical models were suggested to explain them. After a decade of intensive studies of HK/MG, theoretical^{10,11} and experimental¹² studies on Hf-based dielectrics have shown that FLP is not an intrinsic property of a given dielectric. Instead, it was argued that FLP can occur for specific metal-dielectric combinations,¹³ which are therefore termed extrinsic FLP mechanisms.

In the recent decade, many studies on EWF control with metal alloys covering much of the periodic table were published. These studies investigated the EWF either on SiO₂ (Refs. 14–17) or on Hf-based dielectrics (Refs. 18–21). Due to significant thermal stability concerns,²² metal alloys are

usually not considered as candidates for high-temperature (~ 1000 °C) process flows (the gate-first approach), where alternatives such as ultrathin dielectric capping layers^{23,24} and/or refractory metal nitrides^{25,26} are employed for EWF tuning. However, besides the scientific interest in the mechanisms governing their WF, metal alloys may still be relevant for lower temperature process flows such as gate-last processes, back-end devices, and other applications.

First-principles studies of the WF of alloys can be done by employing the density functional theory (DFT). This has, however, several limitations. One of the challenging aspects of such calculations is the construction of a simulation cell that is sufficiently large to represent a real sample but, on the other hand, that can be handled with finite computational resources. When simulating a MOS device, several assumptions need to be made, such as those concerning crystalline structures and orientations, which are not always reasonable in real samples. For these reasons, the work of Magyari-Köpe *et al.*²⁷ is of particular interest, as they calculated the VWF of Al-Ni bilayers as well as the EWF of these structures on (crystalline) SiO₂. Since lattice matching is required for the periodic boundary conditions of the calculation, only a single crystallographic orientation was studied.

A different approach is to use DFT to calculate the VWF of an alloy without simulating a MOS structure. To avoid modeling complicated phases and structures, Xu *et al.* reported a comprehensive VWF study of the Ni-Pt system as a substitutional solid solution.²⁸ In their work, the VWF of the alloys was calculated for different bulk and surface compositions, focusing only on the (001) plane of a single phase (face-centered cubic [fcc]). Niranjana *et al.* reported the VWF calculations of different crystallographic orientations and atomic terminations of the orthorhombic phase of NiGe and PtGe.²⁹ Their results show a small (~ 0.2 eV) VWF dependence on the orientation and termination for this system, calculated for a single phase and a constant composition (50%at.).

Another approach to simplify the problem was suggested by Xu *et al.*,³⁰ which allowed avoiding the possibility of phase

TABLE I. Crystalline structures and dimensions used for the calculations.

Phase	Structure	Space group	a (Å)	c (Å)	JCPDS ^a card
Pt	Cubic	Fm $\bar{3}$ m (225)	3.923	3.923	00-004-0802
Pt ₃ Al	Tetragonal	P4/mbm (127)	5.449	7.814	00-048-1670
PtAl	Rhombohedral	R $\bar{3}$ (148)	15.623	5.305	00-058-0398
PtAl ₂	Cubic	Fm $\bar{3}$ m (225)	5.922	5.922	03-065-2983
Al	Cubic	Fm $\bar{3}$ m (225)	4.049	4.049	00-004-0787

^aJoint Committee on Powder Diffraction Standards.

formation by doping the surface of Ta crystals of various orientations with various amounts of Mo. In other words, by doping the surface of Ta, simulation of different phases of the same system is circumvented once again. These results demonstrate that, for this system, the crystal orientation is more dominant than the surface concentration. However, it should be noted that Ta, similarly to some other body-centered cubic (bcc) systems such as W and Nb, features a large (~ 1 eV) anisotropy of the WF with respect to the crystallographic orientation, even without surface doping.³¹ In contrast, the elemental components of the current work, Pt and Al, feature a relatively small experimental VWF anisotropy³¹ (~ 0.4 eV).

Recently, an analytical model of the WF composition dependence of solid solution alloys was proposed³² and was followed by a detailed experimental study of the Hf-Ni system on HfO₂.³³ The Hf-Ni alloy features solid state amorphization (SSA), and its EWF was found to depend strongly on the surface enrichment of Hf at its interface with the dielectric, rather than on the average composition of the alloy.

Al₂O₃ is an attractive dielectric model system, due to its simplicity, stability, and relevance as a dielectric for high-mobility channel devices,^{34–36} ultrathin dielectric capping layers,³⁷ and a blocking layer for nonvolatile memories.³⁸ In a recent study,³⁹ we used elemental Pt and Al to establish experimentally that no intrinsic FLP exists with an Al₂O₃ gate dielectric. Based on these findings, alloys of Pt and Al are investigated in the current work as metal gates on Al₂O₃, with the aim of understanding the effect of the composition and microstructure on the WF. Since it was proven that no FLP exists with this system, the use of EWF for an alloy WF study is beneficial because the WF is determined at the metal-dielectric interface, which is protected from oxidation. By contrast, in VWF measurements, avoiding the oxidation of the top free alloy surface requires a delicate control of the ambient. However, the Pt-Al system chosen for this work can feature several metallurgical phenomena, including formation of Kirkendall voids in Al (Ref. 40) and SSA up to 220 °C (Refs. 41 and 42). To avoid WF measurement complexities associated with these effects, and especially to avoid the possibility of voids near the dielectric surface,³³ the Al in the current work is deposited on top of Pt/Al₂O₃, and all samples are annealed at 400 °C, resulting in the formation of various intermetallics based on the thickness ratios of the metal bilayers. A detailed analysis of the microstructure of the formed alloys with different compositions is performed. This enables a comparison of the experimental EWF values with a range of 26 VWF values that are calculated by DFT for different crystallographic orientations of the different phases.

II. EXPERIMENTAL

A. First-principles calculations

First-principles calculations of the VWF values at 0 K were performed for fcc structures of Al and Pt and for three intermetallic phases of Pt-Al alloys. The crystalline phases of Pt-Al for which VWF was calculated were determined by the experimental results that are described below in the results section. The crystalline structures used are listed in Table I, and the sizes of the slab models are specified in Table II. The VWF and free surface energies of all the possible different $\{100\}$, $\{110\}$, and $\{111\}$ families and possible atomic terminations of the five phases were calculated.

The calculations were done using DFT,^{43–45} utilizing the Vienna *ab initio* simulation package (VASP),^{46–48} and the MedeA software environment.⁴⁹ The general gradient approximation (GGA) functional was used to express the exchange

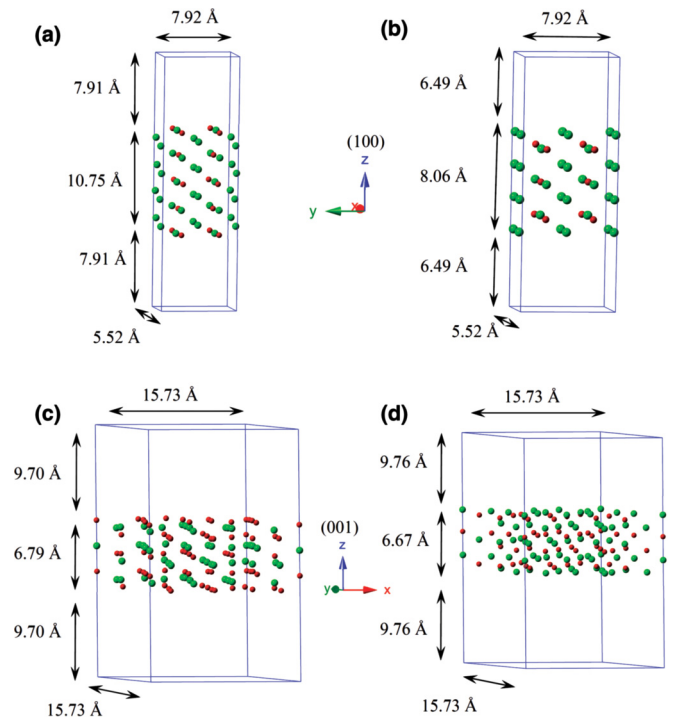


FIG. 1. (Color online) Representative slab models constructed for (a) and (b) (100)-oriented tetragonal Pt₃Al phase and (c) and (d) (001)-oriented rhombohedral PtAl phase. The large (green) and the small (red) points represent Pt and Al atoms, respectively. The figure demonstrates (a) a mixed atomic termination vs (b) Pt atomic termination and (c) Al-terminated vs (d) Pt-terminated planes.

TABLE II. Slab model dimensions and other details.

Phase	Orientation	Termination	Atoms per slab	Unit cell size a,b,c (Å)	Angle, $a-b$ (°)	Number of layers	
Pt	(100)	Pt	8	2.810, 2.810, 25.894	90	8	
	(110)		8	2.810, 3.974, 21.239	90	8	
	(111)		6	2.810, 2.810, 23.765	120	6	
Pt ₃ Al	(100)	Mixed	36	5.521, 7.923, 26.562	90	13	
	(001)		28	5.521, 5.521, 25.847	90	7	
	(110)		56	7.807, 7.923, 25.615	90	10	
	(101)		47	5.521, 9.657, 23.590	90	6	
	(111)		152	17.666, 7.807, 27.510	90	13	
	(100)		Pt	14	5.521, 7.923, 21.041	90	7
	(001)	28		5.521, 5.521, 25.847	90	7	
	(110)	60		7.807, 7.923, 25.615	90	9	
	PtAl	(111)	Mixed	160	17.666, 7.807, 27.510	90	15
(100)		156		5.397, 15.732, 37.249	90	>15 ^a	
(110)		52		5.397, 9.259, 25.732	101.2	>15 ^a	
(101)		67		9.259, 9.259, 85.262	63.7	>15 ^a	
(111)		227		16.631, 16.631, 94.554	70	>15 ^a	
(001)		Pt		117	15.732, 15.732, 26.190	120	9
PtAl ₂	(001)	Mixed	Al	117	15.732, 15.732, 26.190	120	9
	(110)		24	4.203, 5.944, 26.811	90	8	
	(100)		Pt	13	4.203, 4.203, 27.831	90	9
	(111)		13	4.203, 4.203, 30.589	120	13	
	(100)		Al	11	4.203, 4.203, 21.887	90	7
	(111)			15	4.203, 4.203, 30.589	120	15
Al	(100)	Al	4	2.855, 2.855, 18.075	90	4	
	(110)		8	2.855, 4.037, 21.420	90	8	
	(111)		6	2.855, 2.855, 23.986	120	6	

^aThe number of layers is not well defined in these cases due to the low symmetry and complexity of the slab model.

correlation energy, and the projector augmented wave (PAW) potentials were used to calculate the core electrons density.⁵⁰ A plane wave basis set having a 300 eV energy cutoff was used for representing the Kohn–Sham wave functions, and the Brillouin zone was sampled using a uniform Monkhorst–Pack k -point mesh with densities ranging between 0.1 and 0.25 Å⁻¹, depending on the material and the crystallographic orientation. An energy convergence threshold of 10⁻⁵ eV/atom was set, and a threshold of 20 meV/Å Hellman–Feynman⁵¹ force was set for atomic structure relaxation, when allowed.

The computational procedure was divided into three stages. First, all the five bulk phases were relaxed employing the GGA energy functional, allowing the unit cells to reach their equilibrium volumes. Second, various slabs of each phase were constructed, each one representing a certain crystallographic orientation (Table II). Then, the atomic structures of all slabs were relaxed, allowing local atomic movements for surface reconstruction. Third, the VWF values and the surface free energies were calculated for all slabs, with all atoms fixed at their equilibrium positions. The following section describes our computational procedure in detail.

For an accurate VWF calculation, all the slab models were reconstructed with at least six atomic rows each, depending on the surface orientation. The thickness of the vacuum layer is determined to be >10 Å (Refs. 33 and 52–55). Varying the vacuum thickness between 5 to 20 Å in one slab model [nonrelaxed (100) PtAl₂ with a Pt-terminated plane] demonstrated a convergence within 1 meV for vacuum

thicknesses ≥ 7.5 Å. Figure 1 shows a representation of some of the slabs with different orientations, sizes, and atomic terminations.

The slab models were relaxed prior to surface free energy calculations to allow local atomic movements, thereby improving the accuracy. It is noteworthy that calculations of the surface free energy were found to be more sensitive to surface relaxation than VWF calculations.³³ For example, the surface free energy of the nonrelaxed Pt-terminated (111) Pt₃Al surface was calculated to be 2.07 J/m², and it reduces by 8.7% following relaxation. Conversely, the respective calculated VWF values changed by only 0.75% (Table III).

Vacuum work function calculations are based on the plane-averaged electrostatic potentials, which were obtained from the solution of Poisson’s equation for the electronic charge densities,⁵² with the latter directly given as the self-consistent solution of the Kohn–Sham equations. The VWF was calculated as the difference between the vacuum level E_{vac} and the Fermi energy E_F .

The surface free energies were calculated using the relationship between the total molar formation energy of a slab E_{slab}^f and that of a pure bulk material E_{bulk}^f . This allows calculating the surface energy γ as follows:⁵⁶

$$\gamma = \frac{n}{2A} (E_{\text{slab}}^f - E_{\text{bulk}}^f), \quad (1)$$

where n is the number of moles in a slab and A is the surface area. Herein, the formation energies E^f were utilized, rather

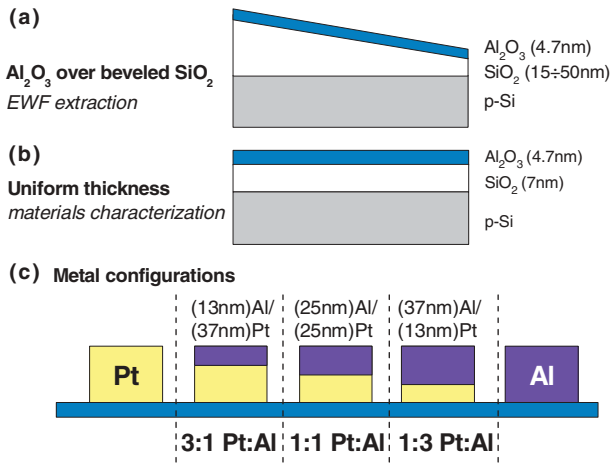


FIG. 2. (Color online) Schematic cross sections of (a) the beveled oxide sample, (b) uniform SiO₂/Si thickness sample, and (c) the different metal electrodes.

than the internal energies (e.g. Ref. 33), to consider the cases of the PtAl₂, Pt₃Al, and PtAl stoichiometric compounds. In these cases, the stoichiometry changes due to construction of slab models. The formation energy of an Al_pPt_q compound is defined as:

$$E_{\text{Al}_p\text{Pt}_q}^f = E_{\text{Al}_p\text{Pt}_q} - p \times \mu_{\text{Al}}^\circ - q \times \mu_{\text{Pt}}^\circ, \quad (2)$$

where $E_{\text{Al}_p\text{Pt}_q}$ is the internal energy of the compound, and μ_{Al}° , μ_{Pt}° are the chemical potentials of the pure Al and Pt in their standard states.⁴⁹

B. Sample fabrication

A beveled oxide structure was formed by a gradual immersion of half 8" (100) p-type Si wafer ($B \sim 3 \times 10^{15} \text{ cm}^{-3}$) with 50 nm of thermal oxide in a dilute (1:10) hydrofluoric (HF) acid. The substrate was then thoroughly washed in deionized water. A 4.7-nm-thick Al₂O₃ layer was then deposited by atomic layer deposition (ALD) on the beveled oxide [Fig. 2(a)] and on 7-nm SiO₂/Si [Fig. 2(b)] substrates using trimethyl aluminum (TMA) and H₂O at 300 °C. Metal-oxide semiconductor capacitors were formed by electron-beam (e-beam) evaporation of Pt and Al layers through a shadow mask ($P < 10^{-7}$ Torr). Figure 2(c) schematically depicts the metal combinations, with the name of the samples derived from the Pt/Al thickness ratio. Given the similar molar volumes of Pt and Al (9.10 and 9.99 cm³/mol, respectively), the molar concentrations of the samples are close to the volume fractions of the deposited layers, namely 77, 56, and 27 ± 7 (Pt at.%) for the 3:1, 1:1, and 3:1 Pt:Al samples, respectively.

The substrates with a uniform thickness [Fig. 2(b)] were used for microstructure analysis. Therefore, no shadow mask was used during the metal deposition on these uniform samples. Postdeposition annealing was done for 30 min at 400 °C in vacuum ($P < 10^{-7}$ Torr) for all samples.

C. Electrical and microstructure characterization

Capacitance-voltage (C-V) measurements were done in a light-sealed chamber using an HP 4284A LCR meter at 100 KHz. The area of each capacitor was measured using an

optical microscope. X-ray diffraction (XRD; Rigaku SmartLab X-Ray Diffractometer) measurements were done in a glancing mode and in a θ - 2θ mode. Glancing mode spectra were collected at 3° from the surface of the blanket metal samples deposited on Al₂O₃ over a uniform thickness SiO₂. These spectra were collected with a Ge-monochromated Cu K α ₁ beam (0.15406 nm) in 0.01° steps at a rate of 1.5°/min and at a rate of 1°/min for the Al-only sample due to its lower atomic scattering factor. The θ - 2θ spectra were collected with a Cu K β filter in 0.01° steps at a rate of 0.6°/min. Transmission electron microscopy (TEM) imaging was done in high-resolution (HR) and in dark field (DF) modes using a monochromated FEI Titan 80-300 TEM operated at 300 KV. The TEM sample preparation was done using a focused ion beam (FIB) on annealed capacitors covered with a protective ~100-nm-thick Ti layer deposited by e-beam evaporation.

III. RESULTS AND DISCUSSION

A. Microstructure results

Glancing mode XRD spectra were used for the identification of the metallic phases of all samples. Figure 3 presents the XRD spectra of all samples with the intensity normalized with respect to the largest peak of each spectrum. Peak identification was done against the highest quality (termed "star") Joint Committee on Powder Diffraction Standards (JCPDS) references specified in Table I. The metallurgical complexity of the samples unfolded with the identification of a tetragonal Pt₃Al in the 3:1 Pt:Al sample, a combination of a rhombohedral PtAl and a tetragonal Pt₃Al in the 1:1 Pt:Al sample, and a cubic PtAl₂ in the 1:3 Pt:Al sample.

The electrode's EWF is determined by the metal in contact with the dielectric. Since the samples were deposited as a bilayer structure and then reacted by annealing, it was important to determine what phase or phases were in contact with the dielectric in the phase-mixture (1:1) alloy. One possibility was the formation of a bilayer structure of the two phases with only one phase in contact with the dielectric, thus determining the EWF. Alternatively, any other grain

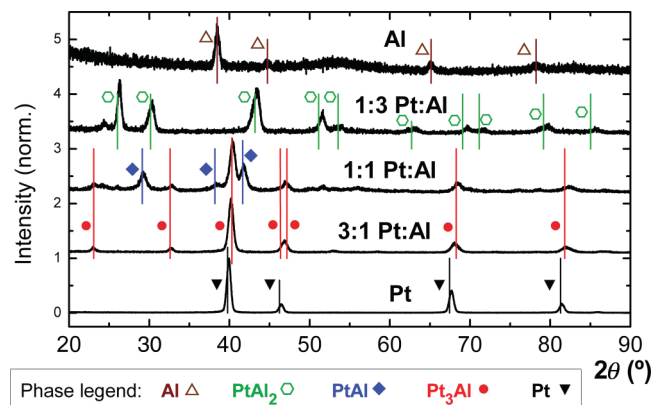


FIG. 3. (Color online) Glancing mode XRD spectra of all samples, each normalized with respect to its largest peak. Vertical lines are positioned in accordance with the appropriate JCPDS reference for the phases specified in the legend and in Table I.

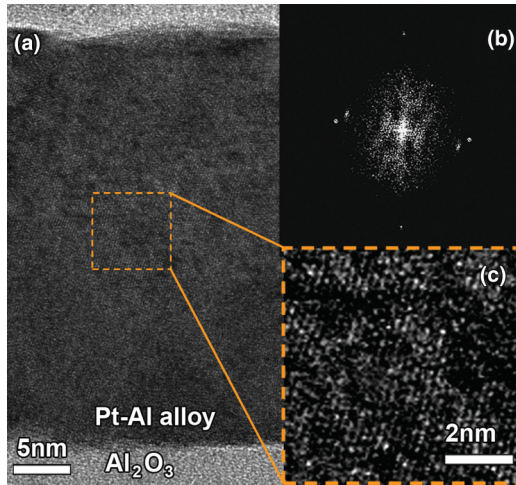


FIG. 4. (Color online) (a) A cross-section HRTEM micrograph of a 1:1 Pt:Al sample showing the full thickness of the layer, (b) an FFT analysis of the larger image, and (c) a $3\times$ enlarged segment of the larger image presented at a different contrast.

arrangement of the two phases was expected to result in a combination of the EWF values of both phases.

To determine what microstructure arrangement was more reasonable, a cross-section TEM sample was imaged at HRTEM and DF modes. Figure 4(a) shows a phase contrast image of the alloy with a continuous pattern of lattice fringes throughout the thickness of the layer; Fig. 4(b) shows a corresponding fast Fourier transform (FFT) further supporting a single grain through the thickness of the entire layer. An enlarged $3\times$ segment of Fig. 4(a) is shown at a different contrast in Fig. 4(c) in order to present the phase contrast more clearly. It should be noted that such high-magnification images are very local, and despite the fact that in many regions of the sample only one or two grains appear per image, these results by themselves cannot be confidently considered as typical for the entire layer.

To gain a wider view, DF imaging was employed at a lower magnification. Figure 5 shows a representative DF image with several grains in Bragg condition.⁵⁷ Similar to the phase contrast image of Fig. 4, the grains' heights span the entire thickness of the alloy layer. Unlike the higher-magnification HRTEM images, in DF, it was possible to obtain a relevant contrast while observing larger regions of the order of $1\ \mu\text{m}$. Therefore, the DF results were considered representative of the entire layer, indicating that the grains of different phases were laterally mixed and not stacked.

In addition to the previous observations, the occurrence of a preferred orientation in the metal layers can influence the EWF as well. In an XRD spectrum collected at a θ - 2θ condition, the preferred orientation of a given hkl crystal orientation P_{hkl} is given by:

$$P_{\text{hkl}} = \frac{I_{\text{hkl}}}{\sum I_{\text{hkl}}} \frac{\sum I_{\text{hkl}}^{\text{ref.}}}{I_{\text{hkl}}^{\text{ref.}}}, \quad (3)$$

where I_{hkl} is the intensity of the given peak, $I_{\text{hkl}}^{\text{ref.}}$ the relative intensity of the powder diffraction reference and the summation is for all the available peaks.

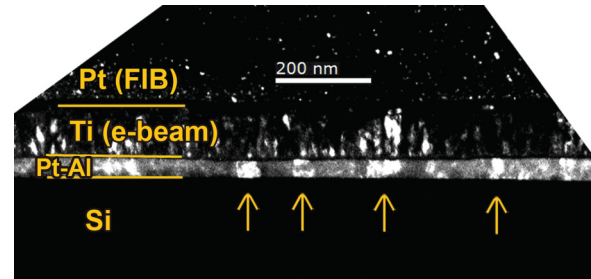


FIG. 5. (Color online) A dark-field (DF) cross-section TEM micrograph of a 1:1 Pt:Al sample showing a bright diffraction contrast from several grains highlighted with arrows.

The θ - 2θ XRDs were collected from all samples (not shown here), and the preferred orientation values calculated from the peak areas using Eq. (3) are summarized in Table IV. It should be noted that, where no preferred orientation was observed, it was impossible to determine whether it did not exist or was below the sensitivity of the measurement at these conditions.

B. Calculation results

Having determined what the main phases of the different samples were, first-principles calculations of the VWF values were applied for each phase independently. The lattice parameters of the pure fcc Pt and Al structures were calculated to be $a = 3.9736\ \text{\AA}$ and $a = 4.0374\ \text{\AA}$, respectively. The parameters of the cubic PtAl_2 and the tetragonal Pt_3Al calculated to be $a = 5.9438\ \text{\AA}$; and $a = 5.5207\ \text{\AA}$ and $c = 7.9234\ \text{\AA}$, respectively, and the calculated rhombohedral PtAl phase was found to be $a = 15.7320\ \text{\AA}$ and $c = 5.3966\ \text{\AA}$. All these values correspond well to the experimental room-temperature values specified in Table I.

The VWF and free surface energies of all the possible different $\{100\}$, $\{110\}$, and $\{111\}$ families and possible atomic terminations were calculated, with the results summarized in Table III. The calculated VWF values of elemental Al and Pt show a good agreement with the literature calculated⁵⁸ and experimental³¹ values, providing further confidence in the DFT results.

Some trends can be observed in the calculated VWF values in Table III. First, the range of values is relatively small, spanning a maximum 0.4–0.6 eV for all the orientations and terminations of a given phase. This indicates a low anisotropy in the VWF, in contrast with results obtained for the Mo-Ta (bcc) system.³⁰ When the different atomic terminations are considered, the following trends appear: in general, the Pt termination behaves similarly to the mixed termination, while the Al termination (where possible) shows a lower VWF, which is the lowest VWF possible for a given structure. In other words, this means that Pt atoms at the surface are more dominant than Al atoms in determining the VWF.

In addition to the VWF, Table III details the surface energies of the different phases, orientations, and atomic terminations. Comparison of the calculated surface energies with the experimental preferred orientations of the phases (Table IV) reveals that the observed crystallographic orientations are not necessarily those with the lowest surface energy, as might have been expected in equilibrium. Indeed, the lowest surface

TABLE III. Calculated VWF values vs literature calculated and experimental values, calculated surface energies for different phases, orientations, and atomic terminations (slab model details are specified in Table II).

Phase	Orientation	Termination	VWF ^a (eV)	Literature VWF (eV)		γ (J/m ²)
				Calc. ^b	Exp.	
Pt	(100)		5.78	5.66	5.75 ^c	1.746
	(110)	Pt	5.28	5.26	5.35 ^d	1.841
	(111)		5.76	5.69	5.70 ^e	1.481
Pt ₃ Al	(100)		4.78			1.371
	(001)		4.85			1.443
	(110)	Mixed	4.93			1.336
	(101)		5.07			1.671
	(111)		4.77			1.727
	(100)		4.76			1.212
	(001)	Pt	5.31			2.285
	(110)		4.84			1.746
	(111)		4.93			1.894
	PtAl	(100)		4.61		
(110)		Mixed	4.66			1.767
(101)			4.70			1.455
(111)			4.70			1.718
(001)		Pt	4.79			1.781
(001)		Al	4.34			1.631
PtAl ₂	(110)	Mixed	4.55			1.323
	(100)	Pt	4.45			1.205
	(111)		4.46			1.359
	(100)	Al	3.94			2.132
	(111)		4.15			1.128
	Al	(100)	Al	4.34	4.30	4.41 ^e
(110)			4.09	4.09	4.06 ^e	1.025
(111)			4.07	4.02	4.24 ^e	0.872

^aPresent study.

^bReference 58.

^cReference 59.

^dReference 60.

^eReference 31.

energy (111) plane of Pt is the preferred orientation observed in the Pt sample. For PtAl₂, the observed (111) preferred orientation may be the lowest surface energy of this phase if this plane has an Al termination. On the other hand, the lowest surface energy termination of Pt₃Al is (100) Pt terminated, while the experiment showed a (101) orientation for the 3:1 Pt:Al sample. For Al and Pt₃Al in the 1:1 Pt:Al sample, it was impossible to determine if a preferred orientation existed, and the PtAl phase showed a (131) preferred orientation, which was

TABLE IV. Summary of the preferred orientations of the different phases calculated using Eq. (3).

Sample (phase)	Preferred orientation, P value
Pt (Pt)	(111), 1.85 ± 0.02
3:1 Pt:Al (Pt ₃ Al)	(202), 1.35 ± 0.02
1:1 Pt:Al (Pt ₃ Al)	
1:1 Pt:Al (PtAl)	(131), 1.9 ± 0.2
1:3 Pt:Al (PtAl ₂)	(111), 3.2 ± 0.4
Al (Al)	

not calculated due to the complexity of the required simulation cell, involving more than 1,000 atoms per cell. It is, therefore, concluded that, for these cases, the calculated minimum surface energy is not a realistic prediction of the preferred orientation of the alloy. This is not surprising, since the samples consist of thin films created by a solid-state reaction and are far from equilibrium. In addition, the formation of the microstructure and phases during annealing involves complex kinetics that are beyond the scope of this work, which may contribute other kinetic and energetic considerations for the formation of phases and their orientations.

C. Electrical results

The beveled oxide method⁶¹ is used for the systematic removal of electrostatic contributions to the flatband voltage (V_{FB}), which in turn allows the extraction of the EWF. As described elsewhere,³⁹ V_{FB} can be written as:

$$V_{FB} = \phi_M^{\text{eff}} - \phi_S - \left(\frac{Q_f}{\epsilon_{ox}} \text{EOT} + \frac{1}{2} \frac{\rho_{ox}}{\epsilon_{ox}} \text{EOT}^2 \right) + \Delta, \quad (4)$$

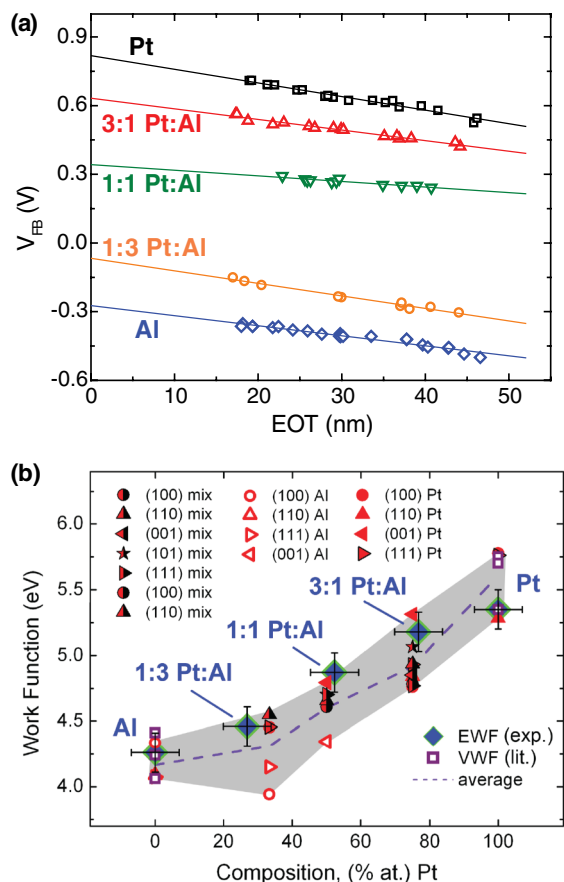


FIG. 6. (Color online) (a) Flatband voltage (V_{FB}) vs EOT curves for Pt, Al, and their alloys. (b) A summary of the experimental EWF (exp.) obtained from the intercepts of Fig. 6(a) and prior knowledge of Δ vs the atomic Pt concentration of the samples. The DFT-calculated VWF of the different phases (Table III) are superimposed on the experimental results in the appropriate composition. The average VWF value for each phase is marked with a dashed line for clarity. In addition, the literature (Ref. 31) VWFs (lit.) for Pt and Al are included. The shaded region represents the possible range of values based on the results.

where ϕ_M^{eff} is the EWF, $\phi_S = k_B T \ln(N_A/n_i) + \chi + E_g/2$ is the semiconductor's WF, with k_B being Boltzmann's constant, T the absolute temperature, N_A the Si doping, n_i the intrinsic carriers concentration, χ the Si affinity, E_g its band gap, Q_f the SiO_2/Si interface charge, EOT the effective oxide thickness, and ϵ_{ox} , ρ_{ox} as the oxide's permittivity and bulk charges, respectively. Here Δ is the net electrostatic contribution of the Al_2O_3 layer to V_{FB} .

The beveled oxide method allows a set of values of EOT to be obtained. Those are used for plotting V_{FB} vs EOT. The cubic term in Eq. (4) is usually neglected for high-quality SiO_2 , as is evident from the linear relationship displayed in Fig. 6(a). Moreover, Δ was found to be 0.4 V in this system³⁹ and in a similar configuration²⁴ corresponding to other reports in the literature.^{62,63} After taking into account these components of Eq. (4), the intercepts of Fig. 6(a) can be used to extract the EWF values of all samples. The EWF values are summarized in Fig. 6(b) vs the overall Pt composition of the sample, with the sample names labeled for clarity.

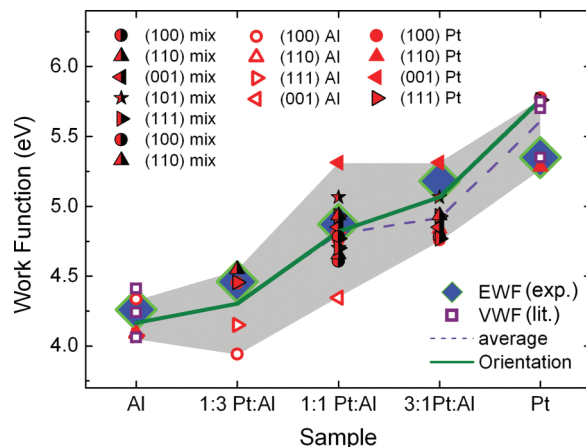


FIG. 7. (Color online) Representation of the Fig. 6(b) data vs the studied samples. Here, the EWF data points are enlarged for clarity to be at the size of their vertical error. The average VWF value and the likely VWF values based on a preferred orientation analysis are shown in lines for clarity.

The EWF values presented in Fig. 6(b) show an incremental and monotonic shift from the lower EWF of Al to the high EWF of Pt. In addition to the experimental EWF data, the calculated VWF values for the different phases (Table III) are superimposed on the same scale with the appropriate composition for each phase. Further, the calculated VWF possibilities for each phase span about ~ 0.5 eV for different orientations and terminations. It is remarkable that the VWF span follows quite well the experimental EWF trend.

While Fig. 6(b) presents the data with respect to the composition of the phases (VWF) and samples (EWF), in Fig. 7 the same WF values are plotted vs the different samples. This means that the VWF values of Pt_3Al and PtAl_2 belong to the 3:1 and 1:3 Pt:Al samples, respectively (see Fig. 3). The VWF values of both the PtAl and Pt_3Al phases are shown at the position of the 1:1 Pt:Al sample. The motivation for rearranging Fig. 6(b) as Fig. 7 is that using a sample axis allows a straightforward comparison of experiment (EWF) and calculations (VWF). Aside from small changes in the horizontal axis between Fig. 6(b) and Fig. 7, the main difference between the two is a slight widening of the range of values of the 1:1 Pt:Al sample in Fig. 7, which is marked by the increased shaded region. However, it is observed again that the trend of the calculated VWF range follows the trend of EWF. Moreover, it can be seen that the majority of the VWF points for each sample are grouped in close proximity to the corresponding EWF. This is also evident from the dashed line in Fig. 7, which represents a simple average of the calculated VWF of each phase. The physical meaning of this average can be regarded as a theoretical VWF value for randomly oriented polycrystalline films. Alternatively, it can be said that considering that many of the points are tightly grouped for each sample, the average makes the contribution of the farther points less dominant.

An additional physical insight can be gained when considering the preferred orientation values summarized in Table IV and carefully combining them with the VWF of Table III. For the Pt sample, the VWF of (111) is taken, as

this is distinctly the preferred orientation. For the 3:1 Pt:Al sample, the (101) mixed-termination VWF is used, being the only termination possible with the (101) preferred orientation. For the 1:3 Al sample, an average of the Pt- and Al-terminated (111) VWF is used, as both are possible for this preferred orientation (and only 0.31 eV apart). In the Al and 1:1 Pt:Al samples, it was not possible to determine if a preferred orientation existed, but the possible VWFs span a range of only 0.25 eV for Al and 0.3 eV for 1:1 Pt:Al (for seven of the eight data points of the latter). Therefore, an average value of the VWF of each of these two samples is the most reasonable option. The values discussed in this paragraph are summarized in Fig. 7 with the thick line denoted “orientation”; the entire range of VWF is for all the possible phases, and the orientation data is a selection of the more likely VWF values based on the preferred orientation data. The correlation between this orientation-based data and the experimental results is surprisingly good, considering the metallurgical-microstructural complexity observed in the Pt-Al system.

The largest deviation between the EWF and the calculated VWF is observed in the Pt sample. The experimental EWF value (5.35 eV) is lower than the calculated (111) VWF (5.76 eV), with the latter corresponding well to the literature experimental (111) value (5.7 eV). Similar values were obtained for the EWF of Pt/SiO₂ in a previous work,³⁹ which is consistent with other works reporting values of (5 ~ 5.22 eV) for Pt/SiO₂ (Refs. 15–17). Moreover, similar EWF were estimated⁹ for Pt/HfO₂ (5.23 eV, based on Ref. 64) and for Pt/ZrO₂ (5.05 eV, based on Ref. 65). The physical origin of this discrepancy is beyond the scope of this work, but it is noted that the EWF obtained here corresponds to the values reported in other works.

IV. SUMMARY AND CONCLUSIONS

This paper describes the combination of three parallel efforts: (a) a comprehensive first-principles study of the VWF of different phases of Pt-Al alloys with different orientations

and atomic terminations, (b) an experimental study of the EWF of these alloys on Al₂O₃ as part of a MOS device using the beveled oxide method, and (c) a detailed microstructural analysis of the samples. The span of the VWF data is shown to behave similarly to the trend of the experimental results. Moreover, with the knowledge of the microstructure, it is shown that it is possible to fine-tune the first-principles predictions of the VWF and to correlate them well with the experimental EWF values. It is further shown that the VWF dependence on the orientation and atomic termination is relatively small (typically well below 0.5 eV) and that Pt atoms in the terminating plane are more dominant in the determination of the WF.

In conclusion, it is shown that the WF of Pt-Al alloys behaves monotonically with the composition, despite the formation of a complex microstructure. The ability of DFT-based calculations to predict the WF of alloys is demonstrated for an array of different phases. The detailed knowledge of the microstructure of the samples is shown to be important for an accurate prediction of the WF.

ACKNOWLEDGMENTS

The authors Y.A. and L.K. contributed equally to this work. The authors thank Boris Meyler for the ALD deposition, Avi Shay for assistance with e-beam deposition, Yaron Kauffman for assistance with the TEM work, Joshua Shechter for assistance with the XRD measurements, and Yechiel Mozes for technical assistance. Tzipi Cohen-Hyams is acknowledged for her expertise and assistance with TEM sample preparation. The authors thank Catherine Cytermann for fruitful discussions. Y.A. wishes to acknowledge René Windiks, Materials Design Inc., for helpful discussions.

Sample preparation for this work was done with the support of the Technion’s Micro-Nanoelectronic Fabrication Unit (MNFU). The work was funded by the ALPHA consortium of the Israeli Ministry of Industry, Trade, and Labor, and by the Russell Berrie Nanotechnology Institute (RBNI) at the Technion.

*Corresponding author: liork@technion.ac.il

¹C. G. Vayenas, S. Bebelis, and S. Ladas, *Nature* **343**, 625 (1990).

²H. M. Mils and M. A. Thomason, *J. Electrochem. Soc.* **123**, 1459 (1976).

³P. Bergveld, J. Hendrikse, and W. Olthuis, *Meas. Sci. Technol.* **9**, 1801 (1998).

⁴Y. Shigehiko, *Rep. Prog. Phys.* **69**, 181 (2006).

⁵R. T. Tung, *Phys. Rev. Lett.* **84**, 6078 (2000).

⁶G. D. Wilk, R. M. Wallace, and J. M. Anthony, *J. Appl. Phys.* **89**, 5243 (2001).

⁷John Robertson, *Rep. Prog. Phys.* **69**, 327 (2006).

⁸John Robertson, *J. Vac. Sci. & Tech. B* **27**, 277 (2009).

⁹Y. C. Yeo, T. J. King, and C. Hu, *J. Appl. Phys.* **92**, 7266 (2002).

¹⁰Koon-Yiu Tse and John Robertson, *Phys. Rev. Lett.* **99**, 086805 (2007).

¹¹K. Y. Tse, D. Liu, and J. Robertson, *Phys. Rev. B* **81**, 035325 (2010).

¹²H. C. Wen, P. Majhi, K. Choi, C. S. Park, H. N. Alshareef, H. Rusty Harris, H. Luan, H. Niimi, H. B. Park, G. Bersuker, P. S. Lysaght,

D. L. Kwong, S. C. Song, B. H. Lee, and R. Jammy, *Microelectron. Eng.* **85**, 2 (2008).

¹³H. N. Alshareef, H. C. Wen, H. F. Luan, K. Choi, H. R. Harris, Y. Senzaki, P. Majhi, B. H. Lee, B. Foran, and G. Lian, *Thin Solid Films* **515**, 1294 (2006).

¹⁴J. Lee, H. Zhong, Y. S. Suh, G. Heuss, J. Gurganus, B. Chen, and V. Misra, *IEEE Elect. Dev. Meeting*, 359, San Francisco, CA (2002).

¹⁵T. L. Li, C. H. Hu, W. L. Ho, H. C. Wang, and C. Y. Chang, *IEEE Trans. Electron Devices* **52**, 1172 (2005).

¹⁶R. M. Todi, A. P. Watten, K. B. Sundaram, K. Barmak, and K. R. Coffey, *IEEE Electron Device Lett.* **27**, 542 (2006).

¹⁷R. M. Todi, M. S. Erickson, K. B. Sundaram, K. Barmak, and K. R. Coffey, *IEEE Trans. Electron Devices* **54**, 807 (2007), <http://ieeexplore.ieee.org/xpl/articleDetails.jsp?tp=&arnumber=4142907>.

¹⁸B. Y. Tsui and C. F. Huang, *IEEE Electron Device Lett.* **24**, 153 (2003).

- ¹⁹M. Sawkar-Mathur and J. P. Chang, *J. Appl. Phys.* **104**, 084101 (2008).
- ²⁰R. P. Birringer, C. H. Lu, M. Deal, Y. Nishi, and R. H. Dauskardt, *J. Appl. Phys.* **108**, 053704 (2010).
- ²¹C.-H. Lu, G. M. T. Wong, R. Birringer, R. Dauskardt, M. D. Deal, B. M. Clemens, and Y. Nishi, *J. Appl. Phys.* **107**, 063710 (2010).
- ²²C. Cabral, C. Lavoie, A. S. Ozcan, R. S. Amos, V. Narayanan, E. P. Gusev, J. L. Jordan-Sweet, and J. M. E. Harperd, *J. Electrochem. Soc.* **151**, F283 (2004).
- ²³M. Bosman, Y. Zhang, C. K. Cheng, X. Li, X. Wu, K. L. Pey, C. T. Lin, Y. W. Chen, S. H. Hsu, and C. H. Hsu, *Appl. Phys. Lett.* **97**, 103504 (2010).
- ²⁴L. Kornblum, B. Meyler, C. Cytermann, S. Yofis, J. Salzman, and M. Eizenberg, *Appl. Phys. Lett.* **100**, 062907 (2012).
- ²⁵H. N. Alshareef, K. Choi, H. C. Wen, H. Luan, H. Harris, Y. Senzaki, P. Majhi, B. H. Lee, R. Jammy, S. Aguirre-Tostado, B. E. Gnade, and R. M. Wallace, *Appl. Phys. Lett.* **88**, 072108 (2006).
- ²⁶C. Adelman, J. Meererschaut, L. A. Ragnarsson, T. Conard, A. Franquet, N. Sengoku, Y. Okuno, P. Favia, H. Bender, C. Zhao, B. J. O'Sullivan, A. Rothschild, T. Schram, J. A. Kittl, S. Van Elshocht, S. De Gendt, P. Lehen, O. Boissière, and C. Lohe, *J. Appl. Phys.* **105**, 053516 (2009).
- ²⁷B. Magyari-Kope, S. Park, L. Colombo, Y. Nishi, and K. Cho, *J. Appl. Phys.* **105**, 013711 (2009).
- ²⁸G. Xu, Q. Wu, Z. Chen, Z. Huang, R. Wu, and Y. P. Feng, *Phys. Rev. B* **78**, 115420 (2008).
- ²⁹M. K. Niranjani, L. Kleinman, and A. A. Demkov, *Phys. Rev. B* **75**, 085326 (2007).
- ³⁰G. Xu, Q. Wu, Z. Chen, Z. Huang, and Y. P. Feng, *J. Appl. Phys.* **106**, 043708 (2009).
- ³¹H. B. Michaelson, *J. Appl. Phys.* **48**, 4729 (1977).
- ³²J. A. Rothschild and M. Eizenberg, *Phys. Rev. B* **81**, 224201 (2010).
- ³³J. A. Rothschild, A. Cohen, A. Brusilovsky, L. Kornblum, Y. Kauffman, Y. Amouyal, and M. Eizenberg, *J. Appl. Phys.* **112**, 013717 (2012).
- ³⁴P. Shekhter, L. Kornblum, Z. Liu, S. Cui, T. P. Ma, and M. Eizenberg, *Appl. Phys. Lett.* **99**, 232103 (2011).
- ³⁵I. Krylov, L. Kornblum, A. Gavrilov, D. Ritter, and M. Eizenberg, *Appl. Phys. Lett.* **100**, 173508 (2012).
- ³⁶R. Zhang, T. Iwasaki, N. Taoka, M. Takenaka, and S. Takagi, *Appl. Phys. Lett.* **98**, 112902 (2011).
- ³⁷H. J. Li and M. I. Gardner, *IEEE Electron Device Lett.* **26**, 441 (2005).
- ³⁸M. Lisiansky, A. Heiman, M. Kovler, A. Fenigstein, Y. Roizin, I. Levin, A. Gladkikh, M. Oksman, R. Edrei, A. Hoffman, Y. Shnieder, and T. Claasen, *Appl. Phys. Lett.* **89**, 153506 (2006).
- ³⁹L. Kornblum, J. A. Rothschild, Y. Kauffmann, R. Brener, and M. Eizenberg, *Phys. Rev. B* **84**, 155317 (2011).
- ⁴⁰Z. Radi, P. B. Barna, and J. Labar, *J. Appl. Phys.* **79**, 4096 (1996).
- ⁴¹B. Blanpain, L. H. Allen, J. M. Legresy, and J. W. Mayer, *Phys. Rev. B* **39**, 13067 (1989).
- ⁴²P. Gas, J. Labar, G. Clugnet, A. Kovacs, C. Bergman, and P. Barna, *J. Appl. Phys.* **90**, 3899 (2001).
- ⁴³R. G. Parr and W. Yang, *Density-Functional Theory of Atoms and Molecules* (Oxford University Press, New York, 1989).
- ⁴⁴R. M. Martin, *Electronic Structure - Basic Theory and Practical Methods* (Cambridge University Press, Cambridge, 2004).
- ⁴⁵Y. Mishin, M. Asta, and J. Li, *Acta Mater.* **58**, 1117 (2010).
- ⁴⁶G. Kresse and J. Furthmuller, *Comput. Mater. Sci.* **6**, 15 (1996).
- ⁴⁷G. Kresse and J. Furthmuller, *Phys. Rev. B* **54**, 11169 (1996).
- ⁴⁸G. Kresse and J. Hafner, *Phys. Rev. B* **49**, 14251 (1994).
- ⁴⁹MedeA v.2.7.4 (Materials Design, Inc., Angel Fire, NM, 2010).
- ⁵⁰G. Kresse and D. Joubert, *Phys. Rev. B* **59**, 1758 (1999).
- ⁵¹R. P. Feynman, *Phys. Rev.* **56**, 340 (1939).
- ⁵²C. J. Fall, N. Binggeli, and A. Baldereschi, *J. Phys.: Condens. Matter* **11**, 2689 (1999).
- ⁵³Y. Amouyal, Z. Mao, and D. N. Seidman, *Appl. Phys. Lett.* **93**, 201905 (2008).
- ⁵⁴Y. Amouyal, Z. Mao, and D. N. Seidman, *Appl. Phys. Lett.* **95**, 161909 (2009).
- ⁵⁵Y. Amouyal, Z. Mao, and D. N. Seidman, *Acta Mater.* **58**, 5898 (2010).
- ⁵⁶H. Zhu, M. Aindow, and R. Ramprasad, *Phys. Rev. B* **80**, 201406 (2009).
- ⁵⁷D. B. Williams and C. B. Carter, *Transmission Electron Microscopy: A Textbook for Materials Science* (Springer, New York, 2009), Chap. 9.3.B.
- ⁵⁸N. E. Singh-Miller and N. Marzari, *Phys. Rev. B* **80**, 235407 (2009).
- ⁵⁹B. Pennemann, K. Oster, and K. Wandelt, *Surf. Sci.* **249**, 35 (1991).
- ⁶⁰R. Vanselow and X. Q. D. Li, *Surf. Sci.* **264**, L200 (1992).
- ⁶¹R. Jha, J. Gurganos, Y. H. Kim, R. Choi, J. Lee, and V. Misra, *IEEE Electron Device Lett.* **25**, 420 (2004).
- ⁶²K. Choi, H. C. Wen, G. Bersuker, R. Harris, and B. H. Lee, *Appl. Phys. Lett.* **93**, 133506 (2008).
- ⁶³Y. Kamimuta, K. Iwamoto, Y. Nunoshige, A. Hirano, W. Mizubayashi, Y. Watanabe, S. Migita, A. Ogawa, H. Ota, T. Nabatame, and A. Toriumi, *Tech. Digest IEDM* (IEEE, Washington DC, 2007), p. 342.
- ⁶⁴L. Kang, B. H. Lee, W. J. Qi, Y. Jeon, R. Nieh, S. Gopalan, K. Onishi, and J. C. Lee, *IEEE Electron Device Lett.* **21**, 181 (2000).
- ⁶⁵W. J. Qi, R. Nieh, B. H. Lee, L. Kang, Y. Jeon, and J. C. Lee, *Appl. Phys. Lett.* **77**, 3269 (2000).